High-quality local pseudopotentials for metals

Yu-Chieh Chi[†] and Chen Huang*,[‡]

†Information Technology Services, California NanoSystems Institute, Center for Scientific Computing, University of California, Santa Barbara, California 93106, United States ‡Department of Scientific Computing, Materials Science and Engineering Program, National High Magnetic Field Laboratory, Florida State University, Tallahassee, Florida 32306, United States

E-mail: chuang3@fsu.edu

Abstract

A major obstacle hindering the application of orbital-free density functional theory (OF-DFT) to all metals is the lack of accurate local pseudopotentials (LPSs), especially for transition metals. In this work, we developed high-quality LPSs for all simple and transition metals by fitting the atomic eigenvalues and the orbital norms beyond cutoff radii. Due to the lack of non-locality in LPSs, it is very challenging to simultaneously fit the semicore and outermost valence orbitals of transition metals. We overcame this issue by excluding the semicore orbitals from the LPS optimizations. This allows us to achieve excellent fittings of the outermost valence orbitals that are responsible for chemical bonding. The norm-conserving condition is then well satisfied, leading to high-quality LPSs. To construct LPSs for magnetic systems, we introduce an additional metric: the atomic spin-polarization energy. By including this metric in the fitting, the LPSs reasonably reproduced many properties of magnetic metals and alloys. The high-quality LPSs developed in this work bring it one step closer to large-scale, reliable OF-DFT simulations of all metals and their alloys.

1 Introduction

Following the Hohenberg–Kohn theorem,¹ the orbital-free density functional theory (OF-DFT)^{2,3} formulates a system's energy only in terms of the electron density. This bypasses the computational complexities in the orbital-based methods, making OF-DFT a promising method for large-scale material simulations. The accuracy of OF-DFT is determined by the kinetic energy density functional (KEDF) which approximates the Kohn-Sham (KS) kinetic energy.⁴ It is challenging to develop a universal KEDF for both metallic and insulating systems, due to the significant difference in their linear response functions.^{5,6} However, OF-DFT should be applicable to all metals, since there is only one bond type: metallic bonds. The capability to perform large-scale, accurate simulations of metals and their alloys will open the door to many exciting applications, such as predicting the magnetic phase diagrams of magnetic alloys⁷⁻¹⁰ and the surface morphology of high-entropy alloy nanoparticles for catalysis.¹¹⁻¹³

For simple metals, high-quality KEDFs based on the linear response function of the free electron gas (FEG) have been developed in the past. ^{14–22} However, developing KEDFs for transition metals is more challenging due to the localized d orbitals. To overcome this obstacle, a density-decomposition scheme was introduced, ²³ which makes it one step closer to applying OF-DFT to all metals. In the scheme, a transition metal's electron density is partitioned into localized and delocalized components. The delocalized component was treated by a FEG-based KEDF. For the localized component, we do not need to compute its kinetic energy, since it is frozen during OF-DFT calculations. The accuracy of this decomposition scheme is mainly determined by the approximation used for calculating the interaction energy between the localized and delocalized densities. It was found that the interaction energy can be reasonably treated even by a linear combination of the Thomas-Fermi ^{24,25} and von Weizsäcker ²⁶ KEDFs, which suggests ample room for improving this scheme. This density-decomposition scheme gave satisfactory predictions for various properties of silver. For the formation energies of Ag-Al alloy, the errors were mainly from silver's local pseudopotentials

(LPSs). This is the motivation for developing highly accurate LPSs in this work: removing the last obstacle for achieving OF-DFT simulations of all metals.

Many methods for constructing LPSs have been developed in the past by fitting against various properties, such as atomic eigenvalues, ^{27–29} atomic orbitals, ³⁰ band structures, ³¹ form factors, ³² binding energies and interstitial electron numbers, ³³ resistivities and Fermi surface distortions. ³⁴ Recently, LPSs were also constructed by fitting other material properties, such as lattice parameters, bulk modulus, relative phase energies, and atomic forces. ^{35–37} Another class of methods inverted LPSs from atomic or bulk electron densities. ^{22,38–46} A recent work integrated non-local pseudopotential into OF-DFT by approximating the non-interacting density matrix with a density functional. ⁴⁷

In this work, we develop a new method for constructing high-quality LPSs for all metals by fitting the atomic eigenvalues and the orbital norms beyond cutoff radii. Our method is inspired by the work of Starkloff and Joannopoulos, ²⁹ who demonstrated that it was possible to approximately reproduce the eigenvalues of the semicore and valence orbitals of a transition metal atom using an LPS. The major difference between their work and ours is that we exclude semicore orbitals from the LPS optimizations. The rationale is that the semicore orbitals do not contribute much to bonding, and their role is only to push the valence orbitals outwards. After excluding the semicore orbitals, we can achieve excellent fittings for the outermost valence orbitals, resulting in high-quality LPSs. Another important development in this work is the introduction of a new metric, the atomic spin-polarization energy, for constructing LPSs for magnetic systems. This metric is defined as the energy difference between the high-spin and low-spin states of an atom. By fitting against this metric, LPSs well reproduce many properties of magnetic systems, such as iron, nickel, and their alloys.

The paper is organized as follows. First, we explain the method for constructing LPSs. We then discuss how to build LPSs for simple and transition metals. The LPSs are tested by calculating various properties of metals and alloys, as well as surface energies, with the

benchmarks from the projector augmented wave (PAW)⁴⁸ calculations. In the end, we show some preliminary results for building an LPS for a lanthanide element cerium and a non-metal element carbon.

2 Theoretical Methods

The first step for building LPSs is to perform all-electron (AE) KS-DFT calculations on an atom. The atom's electron density and KS effective potential are assumed to be spherically symmetric. As a result, the KS orbitals can be separated into the angular and radial components. 49 The next step is to define the valence orbitals for constructing the LPS. Different elements have different choices of valence orbitals. For transition metals, their semicore electrons are included to make sure that the lowest pseudo orbital is of s type. For example, silver's valence orbitals contain its 4s, 4p, 4d, 5s, and 5p orbitals. The definitions of the valence orbitals for all elements are given in the "Supporting Information" (SI).

The atom's KS potential (v_{KS}) is then unsceened by only removing the valence electrons's Hartree and XC potentials as

$$v_{val}(r) = v_{KS}(r) - v_{val,H}(r) - v_{val,XC}(r)$$

$$\tag{1}$$

where r is the radial coordinate. $v_{val,H}$ and $v_{val,XC}$ are the Hartree and XC potentials of the valence electron density, respectively. A cutoff radius r_{cut} is defined. The LPS is required to match v_{val} beyond r_{cut} and is expanded using the Legendre polynomials $\{P_i(t)\}$ inside r_{cut} as

$$v_{LPS}(r) = \begin{cases} v_{val}(r) & r < r_{cut} \\ \sum_{i=0}^{N_{basis}} c_i P_i(t) & r \ge r_{cut} \end{cases}$$
 (2)

where $t = 2r/r_{cut} - 1$ to ensure that t is in the definition domain [-1, 1] of the Legendre polynomials.

The LPS needs to satisfy the following conditions:

$$v_{LPS}(r_{cut}) = v_{val}(r_{cut}) \tag{3}$$

$$v'_{LPS}(r_{cut}) = v'_{val}(r_{cut}) \tag{4}$$

$$v_{LPS}''(r_{cut}) = v_{val}''(r_{cut}) \tag{5}$$

$$v_{LPS}'(0) = 0 (6)$$

$$v_{LPS}''(0) = 0. (7)$$

The first three conditions ensure that v_{LPS} transitions smoothly to v_{val} at r_{cut} . The fourth (zero slope) and fifth (zero curvature) conditions help produce smooth pseudo-orbitals near r=0 in order to reduce the number of plane waves in later DFT simulations. These two conditions are inspired by the Troullier-Martins (TM) scheme. ⁵⁰ The difference is that, in the TM scheme, the conditions are imposed on screened pseudopotentials, while in our scheme the conditions are imposed on unscreened pseudopotentials.

In addition, we also require the LPSs to well reproduce the valence orbitals' eigenvalues $\{\epsilon_i\}$ and the orbital norms beyond r_{cut} , which is achieved by minimizing the cost function F

$$F = \sum_{i} p_{i} (\epsilon_{i}^{AE} - \epsilon_{i}^{PS})^{2} + \sum_{i} q_{i} (N_{i}^{AE} - N_{i}^{PS})^{2}$$
 (8)

where i runs over all valence orbitals. p_i and q_i are weight coefficients. N_i^{AE} and N_i^{PS} are obtained by integrating $\phi_i^{AE}(r)^2$ and $\phi_i^{PS}(r)^2$ from r_{cut} to ∞ , with $\phi_i^{AE}(r)$ and $\phi_i^{PS}(r)$ denoting the AE and pseudo orbitals, respectively. Note that the norm-matching condition does not ensure the pseudo-orbitals match the AE orbitals beyond r_{cut} . However, in practice, we find that the pseudo-orbitals agree very well with the AE orbitals for $r > r_{cut}$ for nearly all elements, except Fe, Co, Cs, and Ba. For these four elements, we also attempted to build the LPSs without the norm-matching conditions, instead directly matching the pseudo and AE orbitals beyond r_{cut} . The pseudo-orbitals were not improved much. This is actually

expected, since the orbital-matching condition is more difficult to meet than the norm-matching condition. Nevertheless, the mismatching between the pseudo and AE orbitals for these four elements is still acceptable.

In practice, we find that an accurate reproduction of eigenvalues is critical for building high-quality LPSs. Therefore, for cases where it is difficult to simultaneously reproduce both the eigenvalues and the orbital norms, we focus on fitting eigenvalues by reducing q_i (with p_i fixed to 1). How to choose p_i and q_i is discussed in later sections. In Eq. 2, the number of basis functions (N_{basis}) for expanding v_{LPS} is usually equal to the number of terms in F. N_{basis} , r_{cut} , p_i , and q_i for all elements are given in the SI.

With the expansion of v_{LPS} in Eq. 2, F is a function of $\{c_i\}$. In practice, we minimize F against $\{c_0, c_1, \ldots, c_{n-5}\}$, and other coefficients $\{c_{n-4}, c_{n-3}, c_{n-2}, c_{n-1}, c_n\}$ can be solved based on the following linear equations (after inserting Eq. 2 into Eqs. 3-7)

$$\sum_{i=n-4}^{n} c_i P_i(1) = v_{val}(r_{cut}) - \sum_{i=1}^{n-5} c_i P_i(1)$$
(9)

$$\sum_{i=n-4}^{n} c_i P_i'(1)\alpha = v_{val}'(r_{cut}) - \sum_{i=1}^{n-5} c_i P_i'(1)\alpha$$
(10)

$$\sum_{i=n-4}^{n} c_i P_i''(1)\alpha^2 = v_{val}''(r_{cut}) - \sum_{i=1}^{n-5} c_i P_i''(1)\alpha^2$$
(11)

$$\sum_{i=n-4}^{n} c_i P_i'(0) = -\sum_{i=1}^{n-5} c_i P_i'(1)$$
(12)

$$\sum_{i=n-4}^{n} c_i P_i''(0) = -\sum_{i=1}^{n-5} c_i P_i''(0)$$
(13)

with $\alpha = 2/r_{cut}$.

While the above method yields good-quality LPSs for non-magnetic systems, for magnetic systems (e.g., Fe, Co, and Ni) the LPSs from the above method often give inaccurate energy differences among different magnetic phases. This issue can be resolved by introducing an additional metric: the atomic spin-polarization energy (E_m) , which is defined as the energy

difference between an atom's high-spin and non-spin states:

$$E_m = E_{\text{non-spin}} - E_{\text{high-spin}}.$$
 (14)

High-spin states are usually prepared by saturating the spin-up d orbital, with the remaining d electrons assigned to the spin-down d orbitals. The electrons in s and p orbitals are distributed evenly among the two spin channels. More details on preparing high-spin states are given in Section 4.2. The augmented cost function is

$$F = \sum_{i} p_{i} (\epsilon_{i}^{AE} - \epsilon_{i}^{PS})^{2} + \sum_{i} q_{i} (N_{i}^{AE} - N_{i}^{PS})^{2} + w_{m} (E_{m}^{AE} - E_{m}^{LPS})^{2}$$
(15)

where E_m^{LPS} is from the LPS calculations. w_m controls how well E_m^{AE} is reproduced. While a larger w_m improves the fitting of E_m^{AE} , it can deteriorate the fittings of eigenvalues and orbital norms. To achieve a good balance, we gradually increase w_m from zero until E_m^{AE} is reasonably reproduced without significantly deteriorating the fittings of eigenvalues and orbital norms.

3 Numerical Details

LPSs are generated using a modified FHI98PP program. 51 The cost functions defined in Eq. 8 and Eq. 15 are minimized using the limited-memory Broyden–Fletcher–Goldfarb–Shanno method, 52,53 with the gradients calculated using the central finite difference method. All KS-DFT calculations are performed using the Perdew-Burke-Ernzerhof GGA XC⁵⁴ functional. Metals and alloys are calculated using a Fermi-Dirac smearing with a smearing width of 0.1 eV. Benchmarks are calculated using the PAW method using either ABINIT 55,56 or Vienna Ab initio Simulation Package (VASP) programs. $^{57-59}$ GBRV pseudopotentials 60 are used for ABINIT benchmark calculations. The kinetic energy cutoffs are 600 eV and 4000 eV for PAW and LPS calculations. We employ Monkhorst-Pack k-point meshes 61 of $16 \times 16 \times 16$

for body-centered cubic (BCC), face-centered cubic (FCC), and simple cubic (SC) structures, and $12 \times 12 \times 12$ for cubic diamond (CD) and hexagonal close-packed (HCP) structures. For alloys, k-point meshes 61 of $12 \times 12 \times 12$ are used. For surface calculations, k-point meshes 61 of $12 \times 12 \times 12$ are used. The simulation box of each surface is set based on the lattice constants of the corresponding bulk without further relaxation, and the atoms are fully relaxed. For both FCC and BCC surfaces, the (1×1) lateral unit cells are used with seven layers in the z direction. A 10 angstrom vacuum is added to reduce the interaction between periodic images.

4 Results and Discussions

4.1 Build local pseudopotentials for transition metals: the non-spin-polarized case

An LPS is built for a set of valence orbitals. The valence electrons are defined so that the lowest eigenstate is of s type, which is required for any spherically symmetric potential. This means that semicore orbitals need to be included for transition metals. For example, silver's valence orbitals contain its 4s, 4p, 4d, 5s, and 5p orbitals. The general rule is that we select the third and fourth shells for the fourth-row transition metals, the fourth and fifth shells for the fifth-row transition metals, and the fifth and sixth shells for the sixth-row transition metals.

LPSs are constructed by minimizing F defined in Eq. 8. A major step during the minimization is to perform self-consistent KS-DFT calculations on an atom for a trial LPS. If the trial LPS is not very physical, the calculation may diverge. The divergence can be largely avoided by working on a slightly positively charged atom. For example, silver's LPS is built based on the electronic configuration [Kr] $4d^{10}5s^{0.5}5p^{0}$, where [Kr] denotes the electronic configuration of the Krypton atom. The atom is positively charged by 0.5e by setting the occupation number of 5s to 0.5. Nearly all LPSs are built by using slightly positively

charged atoms. Their electronic configurations are given in the SI.

Another challenge is that it is very difficult to effectively minimize F, due to the lack of non-locality in LPSs. To resolve this issue, we have to remove some terms in F. The key observation in this work is that semicore s and p orbitals do not participate much in bonding and can be safely excluded from the LPS optimizations. Taking silver as an example, its 4s and 4p's eigenvalues and orbital norms are not included in the LPS optimization by setting their p_i and q_i parameters to zero. However, the 4s and 4p orbitals are still included as the valence electrons and change as the LPS is optimized. The only role of the 4s and 4p orbitals is to push the outermost valence orbitals (4d, 5s, 4d, 5s) outwards.

Even after excluding semicore s and p orbitals, sometimes the minimization of F can still be difficult, and we need to remove more terms from F. We find that, by setting $q_i = 0$ for the outermost p orbital, F can be effectively minimized. For example, for silver, we set $q_i = 0$ for its 5p orbital. This still produces highly accurate LPSs, which should be due to the fact that the outermost p orbitals of transition metals have zero occupation numbers and contribute less to bonding than the outermost s and s orbitals. Note that the eigenvalue of the outermost s orbital is still included in the fitting. Let's summarize the settings for silver: (a) the semicore s and s orbitals (s and s orbitals (s and s orbitals are fitted by setting their s one; (b) the eigenvalues of s orbitals are fitted by setting their s one; (c) the outer norms of s or s or s or s or s or s orbitals are fitted by setting their s one; (c) the outer norms of s or s o

Figure 1(a) shows silver's LPS. By construction, v_{LPS} matches v_{val} beyond $r_{cut} = 2$ Bohr. Inside r_{cut} , v_{LPS} is repulsive because the valence orbitals undergo the following pseudization: $4s \to 1s$, $4p \to 2p$, $4d \to 3d$, $5s \to 2s$, and $5p \to 3p$. Therefore v_{LPS} only needs to push the pseudo orbitals out of the core region. Figure 1(b) and (c) compare the AE and pseudo orbitals. Since 4s and 4p orbitals are not included in the fitting, the agreement between AE and LPS is not very good. On the other hand, the 4d and 5s orbitals beyond r_{cut} are well

reproduced by the LPS. Note that even if the outer norm of the 5p orbital is not included in the fitting, it is still well reproduced by the LPS.

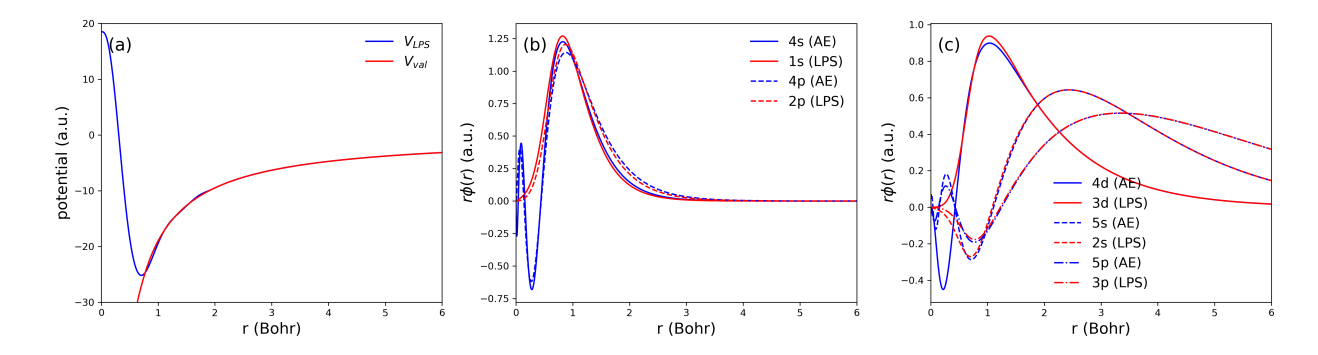


Figure 1: (a) Silver's LPS and unscreened AE valence potential. (b) Silver's 4s and 4p orbitals from AE and LPS calculations. (c) Silver's 4d, 5s, and 5p orbitals from AE and LPS calculations.

Table 1 compares the eigenvalues, the orbitals at r_{cut} , and the orbital norms beyond r_{cut} from AE and LPS calculations. The 4s and 4p orbitals are poorly reproduced by the LPS, since they are not included in the LPS optimization. The 4d, 5s, and 5p orbitals at r_{cut} and their outer norms are all well reproduced by the LPS. As a result, the norm-conserving condition ⁴⁹ is nicely satisfied for 4d, 5s, and 5p, leading to a transferable LPS.

Table 1: Eigenvalues (ϵ in eV), $r\phi(r)$ (in a.u.) at $r_{cut}=2$ Bohr, and the norms (N) beyond r_{cut} for silver's 4s, 4p, 4d, 5s, and 5p orbitals from AE and LPS calculations.

	4s	4p	4d	5s	5p
ϵ_{AE}	-98.980	-62.511	-11.368	-7.715	-3.344
ϵ_{LPS}	-109.603	-69.881	-11.368	-7.715	-3.344
$r\phi_{AE}(r)$	0.1528	0.2460	0.5199	0.5899	0.3348
$r\phi_{LPS}(r)$	0.1286	0.2151	0.5201	0.5906	0.3359
N_{AE}	0.9952	0.9843	0.8363	0.1711	0.0486
N_{LPS}	0.9968	0.9888	0.8363	0.1711	0.0458

4.2 Build local pseudopotentials for transition metals: the spinpolarized case

In what follows, we take Fe as an example to discuss the procedure for building LPSs by fitting against the atomic spin-polarization energy (E_m) . Fe's LPS is built for the valence configuration: $3s^23p^63d^{5.5}4s^24p^0$. The atom is charged by 0.5e to avoid possible divergence during the LPS optimization. Similar to the silver case, the semicore 3s and 3p orbitals are excluded in the LPS optimization. p_i is 1 for 3d, 4s, and 4p orbitals. q_i is 0.01, 0.01, and 0.0 for 3d, 4s, and 4p orbitals, respectively. To compute E_m for Fe, we take $[Ar]3d_{\uparrow}^53d_{\downarrow}^{0.5}4s^24p^0$ as the high-spin state and $[Ar]3d_{\uparrow}^{2.75}3d_{\downarrow}^{2.75}4s^24p^0$ as the non-spin state. We then perform AE calculations on these two spin states and obtain $E_m^{AE} = 4.974$ eV.

Figure 2 shows the impact of w_m on the LPS prediction for E_m (denoted as E_m^{LPS}), as well as the energy differences among Fe's BCC, FCC, and HCP structures. By increasing w_m , E_m^{LPS} approaches E_m^{AE} , and in the meanwhile the correct energy ordering of Fe's FCC and HCP structures is restored. The relative energies between these structures are much improved by fitting against E_m .

While a large w_m improves the fitting of E_m , it can worsen the fittings of eigenvalues and orbital norms. In practice, we keep w_m as small as possible. The optimal w_m can be determined based on Figure 2, in which both E_m and the relative energies are not improved much for $w_m > 0.2$. Therefore, the optimal w_m is set to 0.2. This gives $E_m^{LPS} = -4.982$ eV, compared well to $E_m^{AE} = -4.974$ eV. With this w_m , the eigenvalue errors for 3d, 4s, and 4p orbitals are still below 1 meV.

Fe's FCC structure has two competing magnetic phases: a low-spin phase and a high-spin phase. The low-spin phase, with a slightly smaller lattice parameter, is predicted by PAW to be only 4 meV/atom lower than the high-spin phase. Thus, these two phases are excellent examples to show the importance of including E_m in the LPS optimization. Without fitting against E_m , LPS only gives the high-spin phase. After fitting against E_m , the low-spin phase emerges. The LPS prediction for the energy difference between these two phases is 3

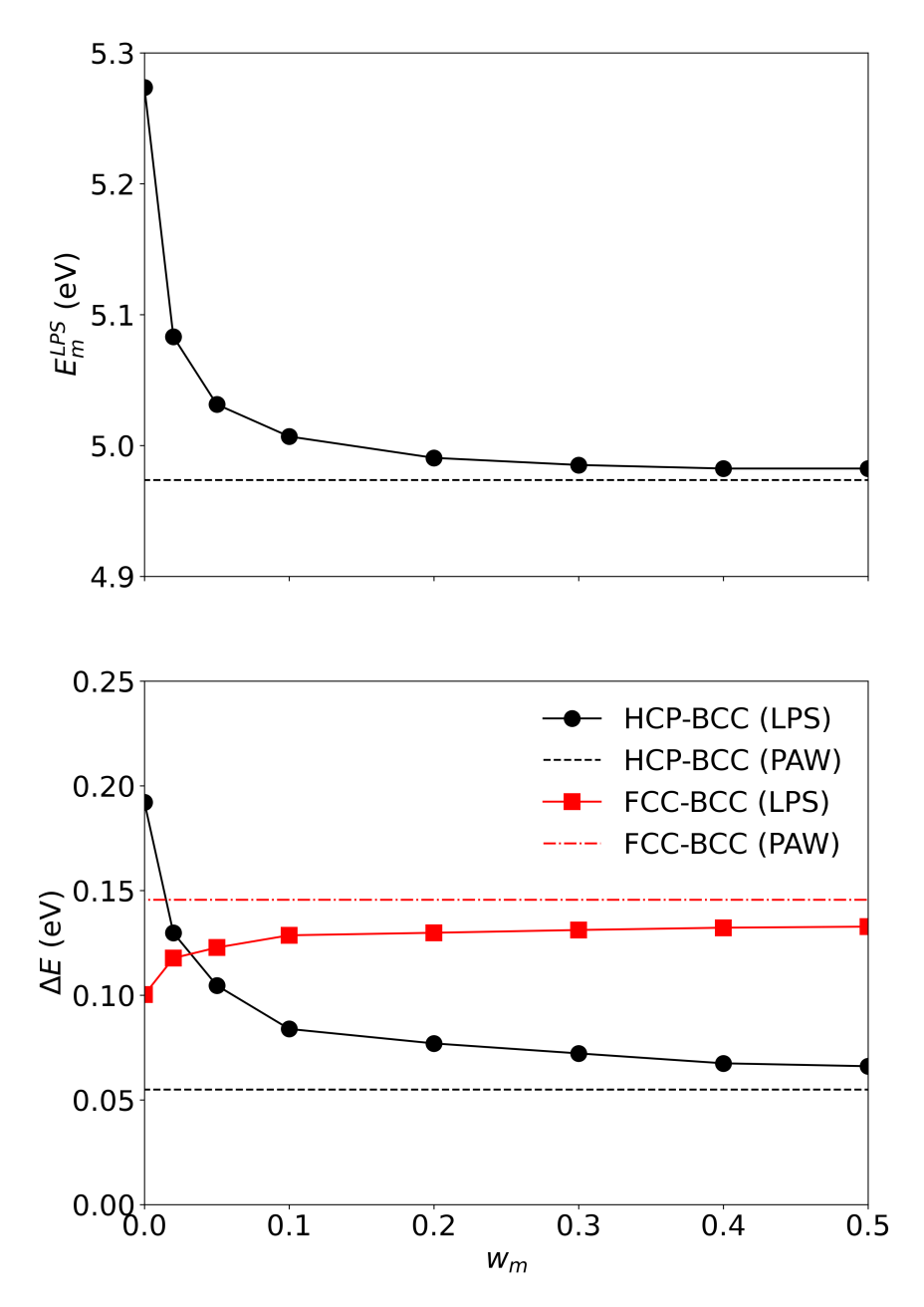


Figure 2: (a) The LPS prediction for E_m as a function of w_m . The benchmark $E_m^{AE} = -4.974$ eV is marked by the dashed lines. (b) The energy difference between Fe's FCC (high-spin) and BCC structures and the energy difference between the HCP and BCC structures, as a function of w_m . The benchmarks from PAW calculations are marked by the dashed lines.

meV/atom, very close to the PAW prediction (4 meV/atom).

The procedure for building LPSs for Co and Ni is similar to Fe. For Co, the high-spin state is $[Ar]3d_{\uparrow}^{5}3d_{\downarrow}^{1.5}4s^{2}4p^{0}$. The calculated E_{m}^{AE} is 3.097 eV. The optimal w_{m} is 0.1, which gives $E_{m}^{LPS}=3.138$ eV. For Ni, the high-spin state is $[Ar]3d_{\uparrow}^{5}3d_{\downarrow}^{2.5}4s^{2}4p^{0}$, and the calculated E_{m}^{AE} is 1.621 eV. Since E_{m}^{LPS} does not change much (only from 1.681 eV to 1.641 eV) against a large variation of w_{m} (from 0 to 1), we then simply set $w_{m}=0$ for Ni.

4.3 Build local pseudopotentials for main group metals

We also have to include the semicore orbitals for defining the valence electrons for the following main group metals: Li, Rb, Cs, Ca, Sr, and Ba. The 1s orbital is included for Li because its 2s orbital has a large overlap with the 1s orbital. For Rb, 4s, 4p, and 4d are included, since its 4d has a higher eigenvalue than its 5s and 5p. For Cs, its 5s, 5p, and 5d orbitals are included, since its 5d's eigenvalue is higher than its 6s and 6p orbitals. For Ca, Sr, and Ba, since their semicore d orbitals have lower energies than the outermost p orbitals, we include 3s and 3p for Ca, 4s and 4p for Sr, and 5s and 5p for Ba. In addition, sometimes we need to set $q_i = 0$ for all valence orbitals to effectively minimize F (see SI for details). Nevertheless, the obtained LPSs are still of high quality.

4.4 Basic properties of metals

We first test LPSs by calculating the basic properties of metals, with the benchmarks from the PAW calculations. The results on lattice constants are summarized in Figure 3. The agreement between LPSs and PAWs is good, with most of the errors within 3%. For transition metals, we observe an interesting zig-zag pattern in these errors. For example, the large positive errors in Figure 3(a) are all from the fourth-row transition metals, the errors of the fifth-row transition metals are closer to zero, and the sixth-row transition metals have the most negative errors. This suggests that the valence electrons of the fifth-row transition metals are more separable from the core electrons and their LPSs are easier to build.

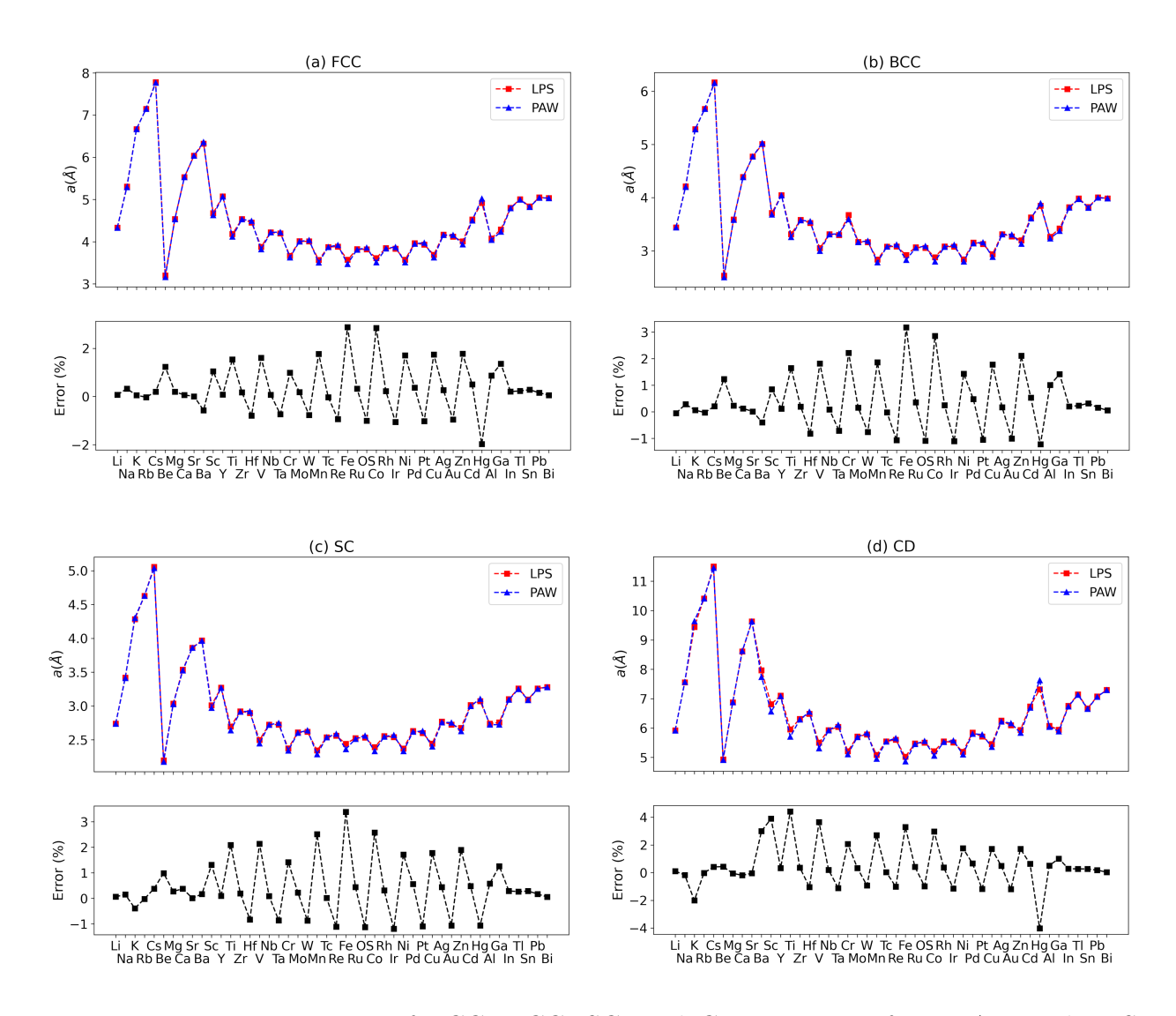


Figure 3: Lattice constants of FCC, BCC, SC, and CD structures from PAW and LPS calculations. The relative errors are calculated as $100 \times (a_{\rm LPS} - a_{\rm PAW})/a_{\rm PAW}$.

Bulk modulus is examined in Fig. 4. A good agreement between LPS and PAW is also observed. For most elements, the relative errors are within 10%. Note that the small moduli of group I and group II metals are well reproduced by the LPSs. Some large errors are seen for the cubic diamond structures of Ba and Sc. This is mainly because their bulk moduli are small. The absolute errors are actually small. For Ba, the LPS and PAW predictions are 6.4 GPa and 4.2 GPa, respectively. For Sc, the LPS and PAW predictions are 8.7 GPa and 12.6 GPa, respectively.

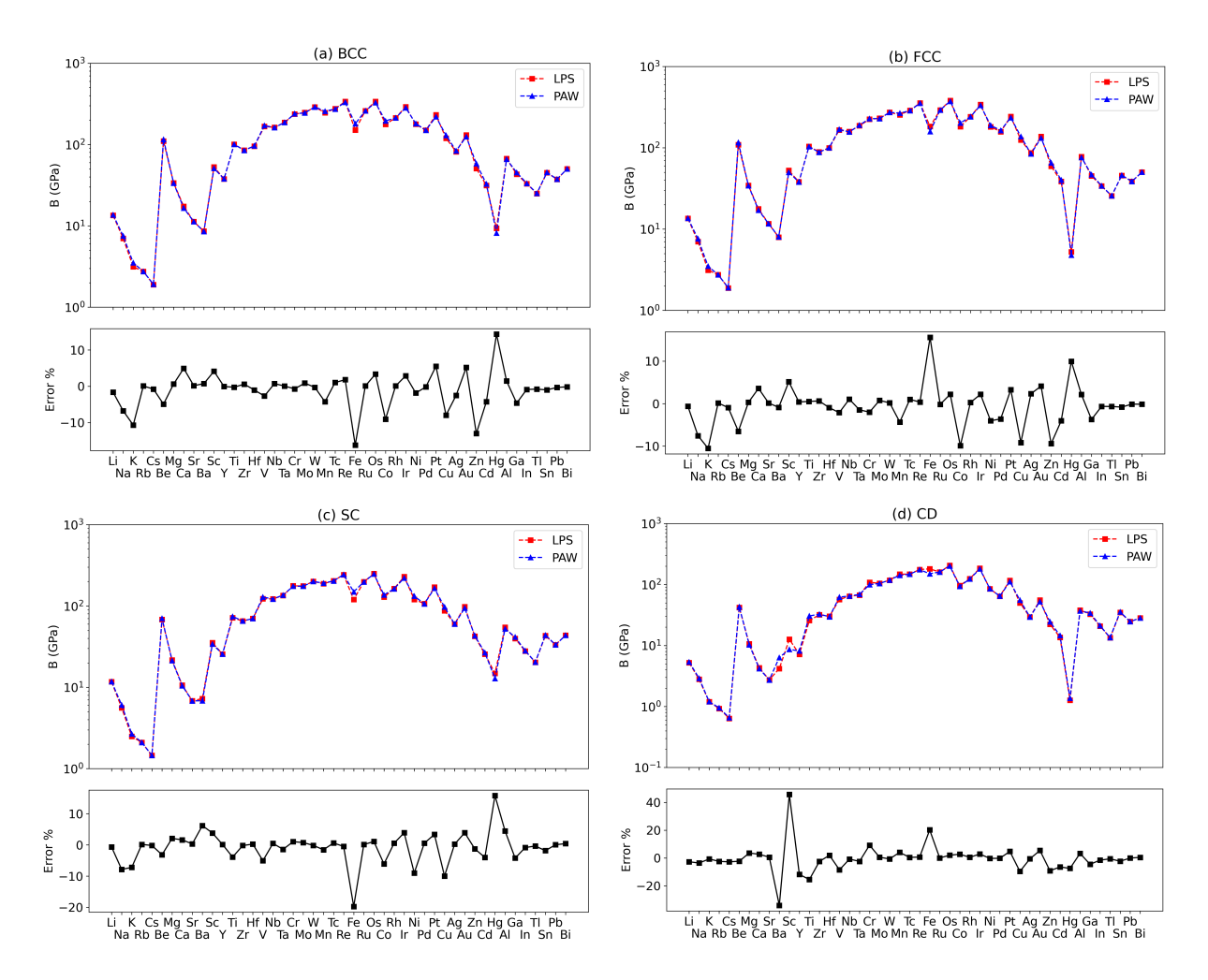


Figure 4: Bulk moduli of FCC, BCC, SC, and CD structures from PAW and LPS calculations. The relative errors are calculated as $100 \times (B_{\rm LPS} - B_{\rm PAW})/B_{\rm PAW}$.

Accurate predictions of the energy differences between different structures are crucial for many applications, such as searching for most stable structures. Table 2 shows the

energies of HCP, BCC, SC, and CD structures, with all referenced to the FCC structures. All calculations are non-spin-polarized, except Fe, Co, and Ni. LPSs well reproduce these energy differences. Particularly, they perform well in many challenging cases, such as the small energy differences between HCP and FCC for group I and II metals, the small energy differences between BCC and FCC for group I atoms, and the small energy differences among Hg's HCP, BCC, and SC structures. For magnetic metals (Fe, Co, and Ni), LPSs are obtained by fitting against E_m and also perform well. They well reproduce the small energy differences between Fe's BCC and HCP, Co's HCP and FCC, and Ni's FCC and HCP.

Table 2: Energies (in eV) per atom of HCP, BCC, SC, and CD structures. All energies are referenced the FCC structures. The mean absolute error (MAE) for each structure is shown at the end.

	Н	CP	В(CC	S	$\overline{\mathbb{C}}$	C	D
	LPS	PAW	LPS	PAW	LPS	PAW	LPS	PAW
Li	-0.0004	-0.0004	0.0020	0.0048	0.1226	0.1228	0.5159	0.5169
Na	0.0002	0.0003	0.0019	0.0020	0.1144	0.1191	0.3233	0.3396
K	-0.0003	-0.0085	0.0003	0.0002	0.0913	0.0960	0.2590	0.2880
Rb	-0.0132	-0.0132	0.0008	0.0008	0.0831	0.0830	0.2507	0.2505
Cs	-0.0003	-0.0003	0.0006	0.0004	0.0944	0.0946	0.2556	0.2588
Be	-0.0872	-0.0870	0.0252	0.0205	0.8620	0.9228	1.4499	1.5553
Mg	-0.0112	-0.0090	0.0212	0.0175	0.3531	0.3674	0.7280	0.7537
Ca	0.0054	0.0072	0.0125	0.0125	0.4053	0.3852	1.0526	1.0305
Sr	0.0050	0.0046	0.0071	0.0070	0.3880	0.3879	0.9524	0.9519
Ba	-0.0024	-0.0022	-0.0085	-0.0105	0.3063	0.3036	0.9719	0.9600
Sc	-0.0488	-0.0485	0.0330	0.0476	0.7286	0.7048	1.9641	1.9333
Y	-0.0331	-0.0314	0.0806	0.0822	0.7591	0.7561	1.9579	1.9487
Ti	-0.0388	-0.0415	0.0505	0.0443	0.8313	0.7752	2.3712	2.2718
Zr	-0.0303	-0.0283	0.0431	0.0407	0.8491	0.8381	2.3827	2.3547
Hf	-0.0531	-0.0527	0.1067	0.1070	1.0172	1.0196	2.6116	2.6078
V	0.0332	0.0070	-0.2045	-0.2416	0.6968	0.6191	2.2747	2.1424
Nb	-0.0356	-0.0326	-0.3274	-0.3236	0.6761	0.6708	2.2322	2.2049
Ta	0.0294	0.0433	-0.2467	-0.2335	0.8992	0.8976	2.6562	2.6558
Cr	0.0227	0.0188	-0.4513	-0.3648	0.6750	0.6502	1.7748	1.7552
Mo	0.0204	0.0251	-0.4094	-0.4064	0.7567	0.7432	1.8380	1.8097
W	0.0156	0.0205	-0.4765	-0.4673	0.9737	0.9733	2.1850	2.1726
Mn	-0.0191	-0.0265	0.0904	0.0784	0.9291	0.8840	1.3632	1.3479
Tc	-0.0622	-0.0628	0.1925	0.1875	1.0185	0.9915	1.4136	1.3756
Re	-0.0683	-0.0615	0.2374	0.2567	1.3446	1.3285	1.5927	1.5611
Fe	-0.0509	-0.0631	-0.1276	-0.1425	0.5532	0.6204	0.9997	1.0939
Ru	-0.0283	-0.0287	0.5064	0.5045	1.0390	1.0257	1.0798	1.0671
Os	-0.0249	-0.0174	0.7633	0.7575	1.4426	1.4071	1.1877	1.1479
Co	-0.0134	-0.0139	0.0756	0.0709	0.7520	0.7044	1.2673	1.1840
Rh	0.0419	0.0417	0.3446	0.3425	0.8104	0.7959	1.1235	1.1014
Ir	0.0828	0.0826	0.6516	0.6281	1.0441	1.0117	1.0248	1.0089
Ni	0.0144	0.0191	0.1018	0.0935	0.6983	0.6895	1.1678	1.1920

Pd	0.0323	0.0357	0.0639	0.0660	0.5365	0.5397	1.1344	1.1397
Pt	0.0773	0.0767	0.1257	0.1200	0.4985	0.4741	1.0746	1.0543
Cu	0.0144	0.0118	0.0364	0.0383	0.4431	0.4784	0.9777	1.0427
Ag	0.0069	0.0031	0.0332	0.0237	0.3362	0.3243	0.7814	0.7645
Au	0.0104	0.0106	0.0254	0.0263	0.2134	0.2077	0.7314	0.7122
Zn	-0.0225	-0.0270	0.0618	0.0649	0.1664	0.2042	0.3871	0.4392
Cd	-0.0098	-0.0107	0.0497	0.0524	0.1156	0.1206	0.3090	0.3250
$_{\mathrm{Hg}}$	-0.0139	-0.0138	-0.0130	-0.0098	-0.0110	-0.0006	0.0747	0.0694
Al	0.0432	0.0386	0.1068	0.0967	0.3506	0.3684	0.7217	0.7315
Ga	0.0180	0.0171	0.0094	0.0150	0.0590	0.0626	0.2408	0.2523
In	0.0102	0.0104	0.0097	0.0093	0.0986	0.0943	0.3320	0.3215
Tl	-0.0156	-0.0143	-0.0124	-0.0125	0.1175	0.1165	0.3507	0.3442
Sn	0.0285	0.0281	0.0170	0.0164	0.0167	0.0133	-0.0554	-0.0500
Pb	0.0276	0.0282	0.0448	0.0447	0.1934	0.1927	0.2695	0.2608
Bi	-0.0270	-0.0254	-0.0517	-0.0514	-0.1356	-0.1347	0.0094	0.0047
MAE	0.0	005	0.0)15	0.0)23	0.0	036

One future goal is to perform large-scale OF-DFT simulations of magnetic alloys. It is then important for LPSs to accurately predict magnetic properties. Table 3 examines the magnetic moments of Fe, Co, and Ni across different structures. For Fe's HCP structure, the type-I antiferromagnetic phase is used. All magnetic moments are well reproduced by LPSs.

Table 3: Magnetic moment (in μ_B/atom) for different structures of Fe, Co, and Ni from LPS and PAW calculations. LS and HS denote the high-spin and low-spin phases of Fe's FCC structure.

		FCC	HCP	BCC	SC	CD
Fe	LPS	1.01(LS), 2.60(HS)	0.0	2.21	2.44	0.0
	PAW	0.95(LS), 2.55(HS)	0.0	2.20	2.39	0.0
Co	LPS	1.67	1.73	1.78	1.87	1.72
	PAW	1.61	1.59	1.73	1.82	1.68
Ni	LPS	0.67	0.71	0.60	0.76	0.82
	PAW	0.60	0.61	0.53	0.57	0.77

4.5 Surface energies

Accurate surface energies are important for predicting the surface morphology of metal nanoparticles, which are promising for catalysis and plasmonics. Table 4 compares LPS and PAW surface energies for four FCC metals (Al, Ni, Cu, and Au) and three BCC metals

(Fe, Cr, and W). For Fe and Ni surfaces, spin-polarized calculations are performed. Overall, LPSs capture the energy ordering of various surfaces.

Table 4: Surface energies (mJ/m^2) calculated using LPSs and PAWs. The PAW results are in parenthesis.

	FCC(111)	FCC(100)	FCC(110)
Al	841 (793)	960 (897)	1022 (1003)
Ni	1812 (1960)	2128 (2182)	2172(2226)
Cu	1225 (1290)	1372 (1441)	1449 (1519)
Au	668 (694)	846 (861)	883 (888)
	BCC(110)	BCC(111)	BCC(100)
Fe	2223 (2366)	2480 (2639)	2280 (2412)
Cr	3155 (3091)	3445 (3383)	3447 (3372)
W	3234 (3180)	3634 (3599)	3892 (3862)

4.6 Alloys

Another future goal is to investigate alloys, especially high-entropy alloys, using OF-DFT. In what follows, we test LPSs on several non-magnetic and magnetic alloys. We are especially interested in the alloy formation energies, which are important for various applications such as calculating the phase diagrams of alloys. Alloy formation energies are calculated as the energy difference between the alloy and the constituent elements in their lowest-energy structures. For simplicity, all alloys take the FCC structure, and a unit cell contains four atoms.

Table 5 and 6 summarize the results for several Cu-based and Fe-based alloys. For Fe-based alloys, all the constituent elements' LPSs are built by fitting against E_m , except for Ti and W for which $w_m = 0$ already gives reasonable E_m . Overall, LPSs yield reasonable alloy formation energies, bulk moduli, magnetic moments, and equilibrium volumes. In particular, the LPSs can successfully predict the magnetic-to-nonmagnetic transition in Ti-Fe alloys as the Ti concentration increases. We also performed extensive tests on Ni-based alloys, with the results summarized in the SI. LPSs also performed satisfactorily in these tests.

Table 5: Formation energies $(E_f, \text{ eV})$, bulk moduli (B, GPa), and the equilibrium volumes $(V_0, \text{Å}^3/\text{cell})$ of several Cu-based binary alloys calculated using LPSs and PAWs. The PAW results are in parentheses. All alloys have the FCC structure. The MAEs are given in the last row. For V_0 , the MAE is for the relative errors.

	E_f	В	$\overline{V_0}$
AlCu ₃	-0.889 (-0.712)	127 (131)	52.05 (50.30)
Al_2Cu_2	-0.790 (-0.593)	110 (111)	55.69 (54.21)
$\mathrm{Al_3Cu}$	-0.285 (-0.158)	93 (92)	62.33 (60.76)
${ m TiCu_3}$	0.328 (0.434)	121 (127)	56.33 (53.97)
$\mathrm{Ti_{2}Cu_{2}}$	-0.214 (-0.195)	122 (126)	60.40(57.12)
${ m Ti_3Cu}$	$0.057 \ (0.011)$	112 (119)	65.93 (62.40)
${ m NiCu_3}$	$0.124\ (0.060)$	144 (152)	48.91 (46.69)
Ni_2Cu_2	$0.268 \; (0.177)$	159(165)	47.73(45.54)
${ m Ni_3Cu}$	$0.254 \ (0.147)$	175 (178)	$46.54 \ (44.56)$
${\rm ZnCu_3}$	-0.205 (-0.267)	119 (126)	52.13 (50.05)
$\mathrm{Zn_{2}Cu_{2}}$	-0.306 (-0.339)	106 (112)	54.85 (52.39)
$\mathrm{Zn_{3}Cu}$	-0.076 (-0.119)	83 (91)	58.29 (55.42)
${\rm ZrCu_3}$	0.269 (0.421)	114 (115)	62.50 (61.25)
$\mathrm{Zr_{2}Cu_{2}}$	-0.634 (-0.499)	116 (116)	70.93 (70.23)
$\mathrm{Zr_{3}Cu}$	$0.034 \ (0.103)$	96 (96)	81.00 (80.53)
$AgCu_3$	$0.239 \ (0.317)$	119 (122)	55.72 (54.02)
Ag_2Cu_2	0.294 (0.389)	109 (110)	61.01 (59.88)
Ag_3Cu	$0.212\ (0.285)$	100 (99)	66.29 (65.78)
SnCu_3	$0.124 \ (0.174)$	102 (107)	60.63 (58.74)
$\mathrm{Sn_{2}Cu_{2}}$	0.679 (0.772)	70 (72)	78.08 (76.49)
$\mathrm{Sn_3Cu}$	0.792 (0.864)	54 (55)	97.03 (95.78)
MAE	0.089	3	3.2%

Table 6: Formation energy $(E_f, \text{ eV})$, bulk modulus (B, GPa), equilibrium volume $(V_0, \text{Å/cell})$, and magnetic moment $(M, \mu_B/\text{cell})$ of Fe-based binary alloys calculated using LPSs and PAWs. The PAW results are in parentheses. All alloys take the FCC structure. The MAEs are given in the last row. For V_0 , the MAE is for the relative errors.

	E_f	В	V_0	M
CoFe ₃	0.342 (0.386)	108 (105)	51.15 (46.01)	9.3 (9.1)
Co_2Fe_2	-0.238 (-0.205)	180 (191)	$49.88 \ (45.87)$	9.0 (8.9)
Co_3Fe	$0.018 \ (0.043)$	183 (195)	$48.23 \ (44.53)$	7.5 (6.9)
$CrFe_3$	0.062 (0.105)	105 (124)	49.31 (44.72)	2.9(2.7)
Cr_2Fe_2	0.389(0.411)	206 (224)	48.97 (44.59)	1.4(1.3)
$\mathrm{Cr}_3\mathrm{Fe}$	$0.854\ (0.925)$	203 (229)	50.69 (45.96)	0.5(0.4)
$MoFe_3$	0.113(0.360)	233 (221)	48.89 (46.99)	1.9(2.1)
Mo_2Fe_2	$0.340 \ (0.670)$	242(227)	53.06 (52.48)	1.5(1.5)
Mo_3Fe	0.927 (1.116)	222(221)	57.76 (58.90)	1.4(1.7)
$CuFe_3$	0.491 (0.494)	125 (137)	50.66 (46.93)	7.5(7.4)
Cu_2Fe_2	$0.583 \ (0.579)$	137 (147)	51.15 (47.85)	5.3(5.3)
Cu_3Fe	$0.850 \ (0.805)$	130 (137)	51.50 (48.67)	2.7(2.6)
$TiFe_3$	-0.694 (-0.363)	124 (141)	52.67 (49.59)	5.5(5.5)
Ti_2Fe_2	-2.054 (-1.622)	192 (197)	53.34 (51.18)	0.0(0.0)
$\mathrm{Ti}_{3}\mathrm{Fe}$	-0.676 (-0.280)	134 (125)	60.23 (59.48)	0.1(0.0)
WFe_3	$0.014 \ (0.219)$	254(243)	49.19 (47.08)	1.8(2.0)
W_2Fe_2	$0.404 \ (0.676)$	266(263)	53.92(52.92)	1.1(0.8)
W_3 Fe	1.099 (1.246)	250 (251)	60.01 (60.01)	1.8(2.1)
$NiFe_3$	$0.147 \ (0.174)$	128 (137)	49.70 (46.06)	8.3 (8.1)
Ni_2Fe_2	-0.235 (-0.210)	172 (180)	$48.48 \ (45.21)$	6.6 (6.4)
Ni ₃ Fe	-0.292 (-0.303)	183 (192)	$47.20 \ (44.50)$	4.9(4.7)
MAE	0.138	10	5.9%	0.17

We also performed tests on several Al-based alloys. We summarized the results below, with the details given in the SI. The LPSs give reasonable predictions, except for the formation energies of Al-Mg and Al-Cr alloys. They are small and challenging to reproduce. PAW (LPS) formation energies of Al₃Mg, Al₂Mg₂, and AlMg₃ are -0.004 (0.035), -0.011 (0.028), and 0.020 (0.046) eV, respectively. While the LPS predictions for Al₃Mg and Al₂Mg₂ are wrong in sign, the energy ordering among these alloys is well reproduced. We have a similar observation for Al-Cr alloys. PAW (LPS) predictions are 0.051 (-0.046), 0.000 (-0.097), and 0.333 (0.225) eV for Al₃Cr, Al₂Cr₂, and AlCr₃, respectively. Again, LPSs give incorrect signs for Al₃Cr and Al₂Cr₂ but correctly reproduce the subtle energy ordering.

Next, we examine the performance of LPSs on several medium-entropy alloys as listed in Table 7. Cu-Zn-Al is a shape-memory alloy. Fe-Co-Ni is a soft magnetic alloy. We also examine alloys formed by randomly choosing four elements from Ag, Au, Cu, Pd, and Pt. This is motivated by recent work on the high-entropy Ag-Au-Cu-Pd-Pt nanoparticles for catalyzing CO and CO₂ reduction reactions. ⁶² Several Fe-Co-Ni-based alloys are also examined. They are related to the Cantor high-entropy alloy (CrMnFeCoNi) ⁶³ and other FeCoNi-based high-entropy alloys. ^{64–67} Since all these alloys are predominantly FCC-type, we employ FCC unit cells in all calculations. For the magnetic alloys, their constituent elements' LPSs are built by fitting against E_m .

Table 7 shows that LPSs well reproduce the bulk moduli and equilibrium volumes for these alloys. It is exciting to see that the magnetic moments are also well reproduced by LPSs. Even though the formation energies of Au-Ag-Pt-Pd-Cu systems are accurately captured by LPSs, we want to point out that the formation energies of AuAgPtPd and CuAgPtPd are small and sensitive to Pt's r_{cut} . If we set r_{cut} to 2.0 Bohr, the LPS formation energies are wrong in sign. Accurate results can be obtained by reducing r_{cut} to 1.5 Bohr. This raises a question: how can one identify the element causing the problem? The trick is to perform calculations with mixed LPSs and non-local pseudopotentials (NLPP). For example, by using NLPP for Au, Ag, and Pd and using LPS for Pt, we can assess the quality of Pt's LPS. If the

Table 7: Formation energy $(E_f, \text{ eV})$, bulk modulus (B, GPa), equilibrium volume $(V_0, \text{Å/cell})$, and magnetic moment $(M, \mu_B/\text{cell})$ of several medium-entropy alloys from LPS and PAW calculations. The PAW results are in parentheses. For non-magnetic alloys, their magnetic moments are marked by "-". The MAEs are given in the last row. For V_0 , the MAE is for the relative errors.

-				
	E_f	В	V_0	M
Cu_2ZnAl	-0.606 (-0.609)	111 (117)	54.78 (52.72)	-
$CuZn_2Al$	-0.114 (-0.102)	86 (89)	59.60 (57.41)	-
$CuZnAl_2$	-0.184 (-0.129)	89 (91)	61.04 (59.18)	-
Fe_2CoNi	-0.063 (-0.029)	169 (172)	49.09 (45.44)	7.5(7.4)
$FeCo_2Ni$	-0.058 (-0.101)	185 (194)	47.79(44.38)	6.5(6.2)
${\rm FeCoNi_2}$	-0.158 (-0.213)	184 (194)	$47.42 \ (44.38)$	5.7(5.6)
AuAgPtPd	-0.029 (-0.026)	154 (156)	66.03 (66.13)	-
AuCuPtPd	-0.234 (-0.215)	167(171)	61.51 (61.14)	-
AuAgCuPd	-0.298 (-0.270)	130 (132)	63.46 (63.18)	-
AuAgPtCu	-0.079 (-0.072)	146 (149)	63.78 (63.34)	-
CuAgPtPd	-0.025 (-0.029)	151 (155)	61.59 (60.83)	-
FeCoNiCr	-0.058 (-0.045)	218 (179)	46.45 (44.75)	0.7(0.8)
FeCoNiMo	-0.054 (0.119)	230(229)	$48.36 \ (46.86)$	0.9(0.9)
FeCoNiCu	$0.181\ (0.196)$	167(176)	48.77 (45.61)	5.1(5.0)
FeCoNiTi	-1.325 (-1.104)	176 (181)	50.17 (47.64)	2.6(2.6)
FeCoNiW	-0.165 (-0.032)	255 (256)	$48.50 \ (46.79)$	0.8(0.7)
FeCoNiMn	-0.026 (-0.070)	163 (171)	$47.98 \ (45.02)$	0.0(0.1)
MAE	0.051	7	3.8%	0.1

formation energy deviates much from the benchmark, Pt's LPS needs to be improved. The easiest way to improve the transferability of an LPS is to reduce its r_{cut} . For FeCoNi-based alloys, the formation energies are reasonably reproduced by the LPSs, except FeCoNiMo. In general, predicting formation energies for magnetic systems is more challenging for LPSs compared to non-magnetic systems.

We also examine the forces from LPS calculations. A Cr₇V₈ alloy, with the BCC structure, is constructed. The unit cell contains 16 lattice sites and 15 atoms, with one Cr atom removed to form a vacancy. The Cr atoms randomly occupy seven lattice sites. The system is first fully relaxed and then a molecular dynamics (MD) simulation is performed at 1000 K with a step size of 2 fs. We take 16 consecutive snapshots from the MD trajectory to examine the total energy per atom and the forces on one Cr atom that is close to the vacancy. Fig. 5(a) shows the total energy per atom. The LPS energy at the first step is shifted to match the PAW energy for a better comparison. After 16 MD steps, the two methods differ by merely 0.01 eV/atom. Fig. 5(b), (c), and (d) show the forces. The deviations between the two methods are much larger than the energy case, due to the fact that forces are more sensitive to the quality of LPSs.

4.7 Preliminary results on lanthanides and non-metal elements

At last, we report some preliminary results on constructing LPSs for lanthanides and nonmetal elements. Lanthanides are useful for many applications, such as rare earth magnets ⁶⁸ and high-performance magnesium-rare-earth alloys. ⁶⁹ For lanthanides, we need to include one more shell for building the LPSs. Taking cerium as an example, its entire fourth shell is included, and the valence configuration is $4s^24p^64d^{10}5s^25p^65d^16s^24f^1$. The reason is that 4f's eigenvalue is lower than 5p. We then need to include the fourth shell to ensure that the lowest p orbital has a lower energy than 4f. We have constructed an LPS for cerium with $r_{cut} = 2.2$ Bohr. Similar to transition metals, only the outermost valence orbitals (5p, 6s, 5d,and 4f) that are responsible for chemical bonding are included in the LPS optimization. The

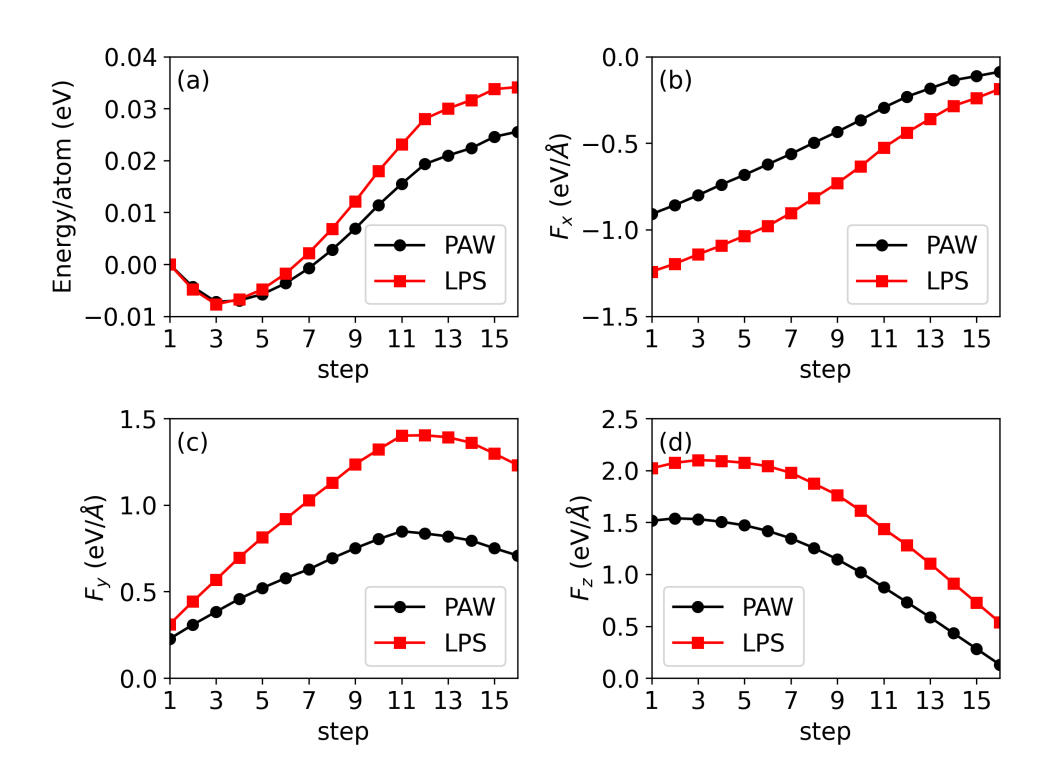


Figure 5: Compare energy per atom and forces for a Cr_7V_8 alloy. The forces are calculated for a Cr atom near the vacancy.

LPS performs well on cerium's FCC, BCC, SC, and CD structures. For bulk modulus, The LPS (PAW) predictions for FCC, BCC, SC, and CD structures are 38 (36), 33 (37), 41 (47), and 56 (69) GPa, respectively. The LPS also well reproduces the energy ordering. The LPS (PAW) predictions for the energy differences $E_{BCC} - E_{FCC}$, $E_{SC} - E_{FCC}$, and $E_{CD} - E_{FCC}$ are 0.197 (0.200), 0.425 (0.337), 0.867 (0.717) eV, respectively. It is encouraging to see that the small energy difference between BCC and FCC is captured by the LPS. In general, the error gradually increases for more open structures (i.e., SC and CD). The LPS errors for the lattice parameters of FCC, BCC, SC, and CD are 1.9%, 1.0%, 3.7%, and 3.3%, respectively. We are still improving the LPS by testing different q_i and r_{cut} values. The final LPSs for lanthanides will be published in a future work.

For non-metal elements, we show some preliminary results for carbon, which is a challenging case due to the strong interaction between the 1s, 2s, and 2p orbitals. Due to this strong interaction, we include the 1s orbital in the valence orbitals for building the LPS. r_{cut} is set

to 0.7 Bohr. The LPS optimization only focuses on fitting 2s and 2p's eigenvalues. The LPS inside r_{cut} is expanded by two basis functions. The eigenvalues of 2s and 2p are reproduced very well by the LPS. The 2s and 2p orbitals outside r_{cut} are reasonably reproduced. This LPS has been tested on the FCC, BCC, SC, and CD structures. The performance is good. The bulk moduli of FCC, BCC, SC, and CD from LPS (PAW) predictions are 108 (107), 157 (159), 316 (310), and 410 (420) GPa, respectively. The energy differences $E_{FCC} - E_{CD}$, $E_{BCC} - E_{CD}$, and $E_{SC} - E_{CD}$ from LPS (PAW) are 4.515 (4.638), 4.246 (4.362), and 2.439 (2.501) eV, respectively. The relative errors for the equilibrium volumes of all structures are within 2%.

5 Conclusion

We have developed high-quality LPSs for the main group and transition metals. The LPSs are required to reproduce the atomic eigenvalues and the outer norms of the valence orbitals. The key finding of this work is that high-quality LPSs for transition metals can be constructed without fitting the semicore orbitals. This lets us achieve excellent fittings for the outermost valence orbitals that are responsible for chemical bonding. The norm-conserving condition is then well satisfied, which leads to high-quality LPSs. Another important development is the introduction of a new metric, the atomic spin-polarized energy, for optimizing LPSs for magnetic systems. Using this metric, LPSs give good predictions for many magnetic systems. All LPSs can be downloaded from an online repository. By combining the high-quality LPSs developed in this work with the previously developed density-decomposition scheme, at now becomes possible to achieve large-scale, sufficiently accurate OF-DFT simulations of all metals and their alloys.

Acknowledgement

This work is supported by the National Science Foundation CAREER award #1752769.

Supporting Information Available

The Supporting Information contains: (a) the parameters $(r_{cut}, p_i, q_i, w_m, \text{ and } N_{basis})$ for defining the cost function F and the configurations of valence electrons for all elements examined in this work, (b) the atomic eigenvalues of all elements from AE and LPS calculations, and (c) the performance of LPSs on Al-based and Ni-based alloys. This material is available free of charge via the Internet at http://pubs.acs.org.

References

- (1) Hohenberg, P.; Kohn, W. Inhomogeneous Electron Gas. *Physical Review* **1964**, *136*, B864–B871.
- (2) Wang, Y. A.; Carter, E. A. *Progress in Theoretical Chemistry and Physics*; Kluwer Academic Publishers, pp 117–184.
- (3) Mi, W.; Luo, K.; Trickey, S. B.; Pavanello, M. Orbital-Free Density Functional Theory: An Attractive Electronic Structure Method for Large-Scale First-Principles Simulations. *Chemical Reviews* **2023**, *123*, 12039–12104.
- (4) Kohn, W.; Sham, L. J. Self-Consistent Equations Including Exchange and Correlation Effects. *Physical Review* **1965**, *140*, A1133–A1138.
- (5) Huang, C.; Carter, E. A. Nonlocal orbital-free kinetic energy density functional for semiconductors. *Physical Review B* **2010**, *81*, 045206.
- (6) Constantin, L. A.; Fabiano, E.; Della Sala, F. Nonlocal kinetic energy functional from the jellium-with-gap model: Applications to orbital-free density functional theory. *Physical Review B* 2018, 97, 205137.
- (7) Sundar, R. S.; Deevi, S. C. Soft magnetic FeCo alloys: alloy development, processing, and properties. *International Materials Reviews* **2005**, *50*, 157–192.

- (8) Entel, P.; Buchelnikov, V. D.; Khovailo, V. V.; Zayak, A. T.; Adeagbo, W. A.; Gruner, M. E.; Herper, H. C.; Wassermann, E. F. Modelling the phase diagram of magnetic shape memory Heusler alloys. *Journal of Physics D: Applied Physics* 2006, 39, 865–889.
- (9) Abrikosov, I. A.; Kissavos, A. E.; Liot, F.; Alling, B.; Simak, S. I.; Peil, O.; Ruban, A. V. Competition between magnetic structures in the Fe rich fcc FeNi alloys. *Physical Review B* 2007, 76, 014434.
- (10) Chaudhary, V.; Chaudhary, R.; Banerjee, R.; Ramanujan, R. Accelerated and conventional development of magnetic high entropy alloys. *Materials Today* 2021, 49, 231–252.
- (11) Xin, Y.; Li, S.; Qian, Y.; Zhu, W.; Yuan, H.; Jiang, P.; Guo, R.; Wang, L. High-Entropy Alloys as a Platform for Catalysis: Progress, Challenges, and Opportunities.

 ACS Catalysis 2020, 10, 11280–11306.
- (12) Kumar Katiyar, N.; Biswas, K.; Yeh, J.-W.; Sharma, S.; Sekhar Tiwary, C. A perspective on the catalysis using the high entropy alloys. *Nano Energy* **2021**, *88*, 106261.
- (13) Li, H.; Lai, J.; Li, Z.; Wang, L. Multi-Sites Electrocatalysis in High-Entropy Alloys.

 *Advanced Functional Materials 2021, 31.
- (14) Chacón, E.; Alvarellos, J. E.; Tarazona, P. Nonlocal kinetic energy functional for non-homogeneous electron systems. *Physical Review B* **1985**, *32*, 7868–7877.
- (15) Wang, L.-W.; Teter, M. P. Kinetic-energy functional of the electron density. *Physical Review B* 1992, 45, 13196–13220.
- (16) Pearson, M.; Smargiassi, E.; Madden, P. A. Ab initio molecular dynamics with an orbital-free density functional. *Journal of Physics: Condensed Matter* **1993**, *5*, 3221–3240.

- (17) Smargiassi, E.; Madden, P. A. Orbital-free kinetic-energy functionals for first-principles molecular dynamics. *Physical Review B* **1994**, *49*, 5220–5226.
- (18) García-González, P.; Alvarellos, J. E.; Chacón, E. Nonlocal kinetic-energy-density functionals. *Physical Review B* **1996**, *53*, 9509–9512.
- (19) García-González, P.; Alvarellos, J. E.; Chacón, E. Kinetic-energy density functional: Atoms and shell structure. *Physical Review A* **1996**, *54*, 1897–1905.
- (20) Wang, Y. A.; Govind, N.; Carter, E. A. Orbital-free kinetic-energy functionals for the nearly free electron gas. *Physical Review B* **1998**, *58*, 13465–13471.
- (21) Wang, Y. A.; Govind, N.; Carter, E. A. Orbital-free kinetic-energy density functionals with a density-dependent kernel. *Physical Review B* **1999**, *60*, 16350–16358.
- (22) Chai, J.-D.; Weeks, J. D. Orbital-free density functional theory: Kinetic potentials andab initiolocal pseudopotentials. *Physical Review B* **2007**, *75*, 205122.
- (23) Huang, C.; Carter, E. A. Toward an orbital-free density functional theory of transition metals based on an electron density decomposition. *Physical Review B* **2012**, *85*, 045126.
- (24) Thomas, L. H. The calculation of atomic fields. *Mathematical Proceedings of the Cambridge Philosophical Society* **1927**, *23*, 542–548.
- (25) Fermi, E. Eine statistische Methode zur Bestimmung einiger Eigenschaften des Atoms und ihre Anwendung auf die Theorie des periodischen Systems der Elemente. Zeitschrift für Physik 1928, 48, 73–79.
- (26) Weizsäcker, C. F. v. Zur Theorie der Kernmassen. Zeitschrift für Physik 1935, 96, 431–458.
- (27) Cohen, M. H. Interatomic interactions in metals. *Journal de Physique et le Radium* **1962**, 23, 643–647.

- (28) Topp, W. C.; Hopfield, J. J. Chemically Motivated Pseudopotential for Sodium. *Physical Review B* **1973**, *7*, 1295–1303.
- (29) Starkloff, T.; Joannopoulos, J. D. Local pseudopotential theory for transition metals. *Physical Review B* **1977**, *16*, 5212–5215.
- (30) Woo, J.; Kim, H.; Kim, W. Y. Neural network-based pseudopotential: development of a transferable local pseudopotential. *Physical Chemistry Chemical Physics* **2022**, *24*, 20094–20103.
- (31) Appelbaum, J. A.; Hamann, D. R. Self-Consistent Pseudopotential for Si. *Physical Review B* **1973**, *8*, 1777–1780.
- (32) Schlüter, M.; Chelikowsky, J. R.; Louie, S. G.; Cohen, M. L. Self-consistent pseudopotential calculations for Si (111) surfaces: Unreconstructed (1×1) and reconstructed (2×1) model structures. *Physical Review B* **1975**, *12*, 4200–4214.
- (33) Fiolhais, C.; Perdew, J. P.; Armster, S. Q.; MacLaren, J. M.; Brajczewska, M. Dominant density parameters and local pseudopotentials for simple metals. *Physical Review B* **1995**, *51*, 14001–14011.
- (34) Ashcroft, N. W. Electron-ion pseudopotentials in the alkali metals. *Journal of Physics C: Solid State Physics* **1968**, *1*, 232–243.
- (35) Legrain, F.; Manzhos, S. Highly accurate local pseudopotentials of Li, Na, and Mg for orbital free density functional theory. *Chemical Physics Letters* **2015**, *622*, 99–103.
- (36) del Rio, B. G.; Dieterich, J. M.; Carter, E. A. Globally-Optimized Local Pseudopotentials for (Orbital-Free) Density Functional Theory Simulations of Liquids and Solids. *Journal of Chemical Theory and Computation* 2017, 13, 3684–3695.

- (37) Lüder, J.; Manzhos, S. Nonparametric Local Pseudopotentials with Machine Learning: A Tin Pseudopotential Built Using Gaussian Process Regression. *The Journal of Physical Chemistry A* **2020**, *124*, 11111–11124.
- (38) González, L. E.; González, D. J.; Silbert, M.; Alonso, J. A. A theoretical study of the static structure and thermodynamics of liquid lithium. *Journal of Physics: Condensed Matter* **1993**, *5*, 4283–4298.
- (39) Watson, S.; Jesson, B. J.; Carter, E. A.; Madden, P. A. Ab initio pseudopotentials for orbital-free density functionals. *Europhysics Letters (EPL)* **1998**, *41*, 37–42.
- (40) Anta, J. A.; Madden, P. A. Structure and dynamics of liquid lithium: comparison of ab initiomolecular dynamics predictions with scattering experiments. *Journal of Physics:* Condensed Matter 1999, 11, 6099–6111.
- (41) González, D. J.; González, L. E.; López, J. M.; Stott, M. J. Dynamical properties of liquid Al near melting: An orbital-free molecular dynamics study. *Physical Review B* 2002, 65, 184201.
- (42) Wang, B.; Stott, M. J. First-principles local pseudopotentials for group-IV elements. *Physical Review B* **2003**, *68*, 195102.
- (43) Huang, C.; Carter, E. A. Transferable local pseudopotentials for magnesium, aluminum and silicon. *Physical Chemistry Chemical Physics* **2008**, *10*, 7109.
- (44) Mi, W.; Zhang, S.; Wang, Y.; Ma, Y.; Miao, M. First-principle optimal local pseudopotentials construction via optimized effective potential method. *The Journal of Chemical Physics* **2016**, *144*.
- (45) Zhou, B.; Alexander Wang, Y.; Carter, E. A. Transferable local pseudopotentials derived via inversion of the Kohn-Sham equations in a bulk environment. *Physical Review B* **2004**, *69*, 125109.

- (46) Zhou, B.; Carter, E. A. First principles local pseudopotential for silver: Towards orbital-free density-functional theory for transition metals. *The Journal of Chemical Physics* **2005**, *122*.
- (47) Xu, Q.; Ma, C.; Mi, W.; Wang, Y.; Ma, Y. Nonlocal pseudopotential energy density functional for orbital-free density functional theory. *Nature Communications* **2022**, *13*.
- (48) Blöchl, P. E. Projector augmented-wave method. *Physical Review B* **1994**, *50*, 17953–17979.
- (49) Hamann, D. R.; Schlüter, M.; Chiang, C. Norm-Conserving Pseudopotentials. *Physical Review Letters* **1979**, 43, 1494–1497.
- (50) Troullier, N.; Martins, J. L. Efficient pseudopotentials for plane-wave calculations. *Physical Review B* **1991**, *43*, 1993–2006.
- (51) Fuchs, M.; Scheffler, M. Ab initio pseudopotentials for electronic structure calculations of poly-atomic systems using density-functional theory. *Computer Physics Communications* **1999**, *119*, 67–98.
- (52) Nocedal, J. Updating quasi-Newton matrices with limited storage. *Mathematics of Computation* **1980**, *35*, 773–782.
- (53) Liu, D. C.; Nocedal, J. On the limited memory BFGS method for large scale optimization. *Mathematical Programming* **1989**, *45*, 503–528.
- (54) Perdew, J. P.; Burke, K.; Ernzerhof, M. Generalized Gradient Approximation Made Simple. *Physical Review Letters* **1996**, *77*, 3865–3868.
- (55) Gonze, X.; Amadon, B.; Anglade, P.-M.; Beuken, J.-M.; Bottin, F.; Boulanger, P.; Bruneval, F.; Caliste, D.; Caracas, R.; Côté, M., et al. ABINIT: First-principles approach to material and nanosystem properties. Computer Physics Communications 2009, 180, 2582–2615.

- (56) Gonze, X.; Amadon, B.; Antonius, G.; Arnardi, F.; Baguet, L.; Beuken, J.-M.; Bieder, J.; Bottin, F.; Bouchet, J.; Bousquet, E., et al. The Abinit project: Impact, environment and recent developments. Computer Physics Communications 2020, 248, 107042.
- (57) Kresse, G.; Hafner, J. Ab initiomolecular dynamics for liquid metals. *Physical Review B* **1993**, 47, 558–561.
- (58) Kresse, G.; Furthmüller, J. Efficiency of ab-initio total energy calculations for metals and semiconductors using a plane-wave basis set. *Computational Materials Science* **1996**, *6*, 15–50.
- (59) Kresse, G.; Furthmüller, J. Efficient iterative schemes forab initiototal-energy calculations using a plane-wave basis set. *Physical Review B* **1996**, *54*, 11169–11186.
- (60) Garrity, K. F.; Bennett, J. W.; Rabe, K. M.; Vanderbilt, D. Pseudopotentials for high-throughput DFT calculations. *Computational Materials Science* **2014**, *81*, 446–452.
- (61) Monkhorst, H. J.; Pack, J. D. Special points for Brillouin-zone integrations. *Physical Review B* **1976**, *13*, 5188–5192.
- (62) Nellaiappan, S.; Katiyar, N. K.; Kumar, R.; Parui, A.; Malviya, K. D.; Pradeep, K. G.; Singh, A. K.; Sharma, S.; Tiwary, C. S.; Biswas, K. High-Entropy Alloys as Catalysts for the CO2 and CO Reduction Reactions: Experimental Realization. ACS Catalysis 2020, 10, 3658–3663.
- (63) Cantor, B.; Chang, I.; Knight, P.; Vincent, A. Microstructural development in equiatomic multicomponent alloys. *Materials Science and Engineering: A* 2004, 375–377, 213–218.
- (64) Chen, T.; Shun, T.; Yeh, J.; Wong, M. Nanostructured nitride films of multi-element high-entropy alloys by reactive DC sputtering. Surface and Coatings Technology 2004, 188–189, 193–200.

- (65) Shaginyan, L. R.; Britun, V. F.; Krapivka, N. A.; Firstov, S. A.; Kotko, A. V.; Gorban, V. F. The Properties of Cr–Co–Cu–Fe–Ni Alloy Films Deposited by Magnetron Sputtering. *Powder Metallurgy and Metal Ceramics* 2018, 57, 293–300.
- (66) Hsu, Y.-C.; Li, C.-L.; Hsueh, C.-H. Modifications of microstructures and mechanical properties of CoCrFeMnNi high entropy alloy films by adding Ti element. Surface and Coatings Technology 2020, 399, 126149.
- (67) Huang, T.-H.; Hsueh, C.-H. Microstructures and mechanical properties of (CoCrFeMnNi)100-Mo high entropy alloy films. *Intermetallics* **2021**, *135*, 107236.
- (68) Coey, J. Perspective and Prospects for Rare Earth Permanent Magnets. *Engineering* **2020**, *6*, 119–131.
- (69) Rochlin, L. L. Magnesium Alloys Containing Rare Earth Metals, 1st ed.; Advances in Metallic Alloys 3; Taylor & Francis: London, 2003.
- (70) Online local pseudopotential repository. https://github.com/chenhuang3/local_pseudopotential_files/.

TOC Graphic